Energy Advances

ROYAL SOCIETY OF CHEMISTRY

PAPER

View Article Online
View Journal | View Issue

Check for updates

Cite this: *Energy Adv.*, 2026, 5, 354

Received 10th October 2025,
Accepted 27th January 2026

DOI: 10.1039/d5ya00293a

rsc.li/energy-advances

# Non-thermal plasma upgrading of humidified $CO_2$ into syngas in a dielectric barrier discharge reactor: tuning $H_2/CO$ ratios *via* specific energy input and gas flow rate

Maxwell Klein and Joshua Jack *

This study investigates the non-thermal plasma (NTP)-driven conversion of humidified $CO_2$ into syngas ($H_2$:CO:$CO_2$) using a dielectric barrier discharge (DBD) reactor. NTP enables $CO_2$ and $H_2O$ dissociation at near-ambient conditions through high-energy electron collisions, eliminating the need for thermal input or expensive catalysts. While prior studies have examined gas composition and humidity effects, the influence of specific energy input (SEI) and gas flow rate on syngas yield and energy efficiency remains underexplored. Here, we systematically evaluate the relationship between SEI, flow rate, energy efficiency, and $H_2$/CO composition. Experiments conducted in a coaxial DBD reactor demonstrate syngas generation with tunable $H_2$/CO ratios ranging from 0.1 to 0.2 with energy efficiencies ranging from 4.5 to 23.3%. Results indicate that higher flow rates enhance energy efficiency, while increasing SEI leads to a plateau in CO and $H_2$ production, suggesting limits in energy transfer efficiency. Overall, these findings can inform the design of next-generation NTP systems towards a circular carbon economy.

## 1. Introduction

The Intergovernmental Panel on Climate Change (IPCC) highlights carbon capture and utilization (CCU) technologies as critical components of a net-zero emissions future.[1] This is particularly relevant for industrial sectors such as cement and steel manufacturing, where $CO_2$ emissions are generated by design (*e.g.*, calcination) and cannot be eliminated by electrification alone.[2] In addition, hard-to-electrify sectors, including aviation and maritime transportation, are likely to rely on carbon-based fuels for the foreseeable future, which could be synthesized from $CO_2$, closing the carbon loop.

Non-thermal plasma (NTP) has emerged as a promising method for low-temperature $CO_2$ conversion into value-added products, offering an electrified route to carbon circularity. In NTP conversion, a high-voltage electric field accelerates free electrons, which can catalyze bond dissociation through electronic excitation, molecular collisions, ionization, or vibrational activation.[3] These systems are classified as "non-thermal" due to the large disparity between electron temperature and bulk gas temperature, enabling highly endothermic reactions such as $CO_2$ and $H_2O$ dissociation to occur near ambient conditions with minimal bulk gas heating.

One promising application of NTP is syngas production from $H_2O$ and $CO_2$. NTP-driven syngas generation can eliminate the need for solid catalysts, reducing system complexity and cost while avoiding issues such as catalyst deactivation, poisoning, or regeneration. Notably, syngas ($H_2$:CO:$CO_2$) can serve as a versatile feedstock for Fischer–Tropsch synthesis of many high-value fuels and chemicals.[4] As such, NTP-driven syngas production could potentially revolutionize industrial chemical manufacturing.

The syngas ratio (*i.e.*, $H_2$/CO molar ratio) can be a crucial parameter for efficient downstream chemical synthesis.[5] Net CO formation *via* NTP typically proceeds through electron impact dissociation of $CO_2$, in a complex reaction network that can be cyclic.[4] Many industrial $CO_2$ streams (*e.g.*, flue gas, cement plant off-gas) also contain water vapor that can not only supply $H^+$ but influence plasma chemistry by introducing additional reaction pathways that produce $H_2$. Notably, net $H_2$ formation occurs by electron impact dissociations of $H_2O$ that create OH and $H^-$, the latter of which collides with $H_2O$ to produce $OH^-$ and $H_2$.[4] Altogether, electron impact dissociations are the primary drivers of syngas formation in NTP. However, many other reaction pathways may also occur, leading to a wide variety of intermediates.[4] In addition, subsequent gas-phase (or surface reactions) can recombine plasma intermediates or unstable gas products like $H_2O_2$ and $HO_2$ back into more stable products such as $H_2$, $CO_2$, or $H_2O$, forming complex reaction clusters.[4]

Overall, the use of NTP to convert humidified $CO_2$ gas into value-added products has only been studied in a handful of

---

*Department of Civil and Environmental Engineering, University of Michigan, Ann Arbor, MI, 48109, USA. E-mail: jdjack@umich.edu*

studies using dielectric barrier discharge (DBD) reactors.[4,6–11] Accordingly, the underlying mechanisms of combined $H_2O$ and $CO_2$ conversion are not well understood.[4] A review conducted by Snoeckx *et al.* finds that $CO_2$ conversion increases with energy input while $H_2$:CO decreases with energy input.[4] The study also finds that $CO_2$ conversion decreases in the presence of $H_2O$ vapor, possibly as a result of destabilization of the plasma discharge[4] or the quenching of vibrational levels of $CO_2$.[4,12,13] For instance, converting $CO_2$ with a water content of 2.05% into syngas at a specific energy input (SEI) of 32 000 J $L^{-1}$, yielded an efficiency of only 7.2%.[4] Still, energy efficiencies remain low (<25%) even when using pure $CO_2$ gas feeds due to a lack of optimization.[14] Besides energy efficiencies, controlling the $H_2$/CO ratio of the syngas is critical for real-world applications, but only a limited range has been demonstrated. Two important operational parameters for achieving both high syngas energy efficiencies and tunable $H_2$/CO ratios could be SEI and gas flow rate. However, no previous studies have systematically studied the impact of these parameters on $CO_2$ and $H_2O$ conversion, presenting a critical gap in research.

To our knowledge, this study is the first to methodically explore the relationship between SEI, energy efficiency, and $H_2$/CO production across a range of fixed gas flow rates in a DBD reactor for syngas production. A key contribution of this work lies in isolating the influence of SEI on syngas composition under otherwise constant operating conditions. In this study, we aimed to demonstrate the feasibility of producing tunable syngas ratios ($H_2$:CO) using a simple, low-cost reactor architecture. From an application standpoint, the ability to control syngas composition by adjusting voltage and flow rate offers a pathway to demand-driven syngas generation from realistic humidified $CO_2$ waste streams. Accordingly, this study holds significant translational potential to improve the efficiency and tunability of humidified $CO_2$ conversion into value-added products, presenting a promising pathway to decarbonizing the chemical and fuel industries.

## 2. Experimental methods

### 2.1. Dielectric barrier discharge reactor setup

A DBD reactor was built, which consisted of a sealed Pyrex tube (outer diameter: 32.4 ± 0.2 mm; inner diameter: 25.5 ± 0.2 mm), functioning as the dielectric barrier, wrapped with a nickel foam electrode (80–120 PPI, 1 mm thick, 114.5 ± 0.2 mm long) connected to ground. Nickel foam was selected for its malleability and ability to maintain a stable electrode morphology after cleaning. Stainless steel mesh, tested initially, was impacted by cleaning and produced non-uniform electric fields that promoted destructive macro-filament formation, compromising discharge stability and reproducibility. A copper rod (22.0 ± 0.2 mm diameter) served as the inner high-voltage electrode, yielding a reaction volume of 32.1 ± 0.3 mL. The inner electrode was connected to a plasma generator that applied a high-frequency oscillating voltage to sustain the plasma discharge (Fig. S1 and Section S1.1).

During each experiment, humidified $CO_2$ was introduced *via* a mass flow controller into the DBD reactor at flow rates of 1.00, 0.20, or 0.04 L $min^{-1}$. High-purity $CO_2$ (bone-dry, >99.9% v/v, Airgas Suppliers) was passed through a humidification vessel (Dioxide Materials) using a mass flow controller (Bronkhorst EL-Flow Select) before entering the reactor. The gas flow rate was continuously monitored upstream of the reactor, with negligible variation over each experiment. Before experimentation, the humidity of the gas was quantified across different flow conditions using a humidity and temperature sensor (DwyerOmega RH-USB series). A detailed description of the humidified gas preparation and measurement procedures is provided in the SI (Section S1.2).

### 2.2. Operation and gas sampling procedure

The plasma discharge was driven by a high-voltage pulsed power supply operating at 500 Hz with a 50% duty cycle, while the pulse oscillation frequency was maintained at 36.5 ± 0.5 kHz. The specific energy input was controlled by adjusting the applied voltage and calculated post-experiment from oscilloscope measurements. The entire setup was enclosed within a custom-built Faraday cage to minimize electromagnetic interference with nearby instrumentation. All experiments began with the reactor equilibrated to ambient room temperature (22 °C). During operation, the humidified $CO_2$ traversed the plasma region and exited from the opposite side of the reactor, where it was collected in a gas sampling bag. Humidified $CO_2$ was flowed for ≥5 minutes to flush the system and stabilize humidity and gas conditions. Prior to plasma ignition, all equipment, including a gas chromatograph (GC), gas bag, thermal imager, and oscilloscope, was prepared for immediate data collection. The plasma generator was initiated at 50 V, and the frequency knob was tuned to maximize current. Voltage was then adjusted to the target value. Once the voltage stabilized, the timer was reset, and data collection proceeded according to a standardized timeline. After five minutes, a thermal image was captured; gas was collected for two minutes, and the oscilloscope recorded current and voltage traces over ≥10 pulses (0.02 s). Resistance and capacitance measurements followed. After seven minutes, final thermal images were taken, and the gas bag was sealed. A 150 ± 1 μL gas sample was then extracted from the gas bag using a Hamilton syringe and injected into an Agilent 8890 GC with a Shincarbon ST column and thermal conductivity detector. Additional details related to the reactor operation and sampling procedure are provided in Section S1.1–1.3.

### 2.3. Gas chromatography

Gas chromatographer (GC) analyses targeted $H_2$, CO, $CO_2$, $N_2$, $O_2$, and $CH_4$. A custom method employed a 20 mL $min^{-1}$ flow rate and a temperature ramp from 200 °C to 135 °C (75 °C $min^{-1}$) to resolve closely eluting $N_2$/$O_2$ peaks. Additional details related to gas analysis are provided in Section S1.3. Calibration was performed using certified gas standards for all species. Species concentrations (mol%) were converted to molar flow rates using the ideal gas law. These values were used to compute $CO_2$ and $H_2O$ conversion, $H_2$/CO product ratios, and energy efficiency. Propagated errors included GC calibration uncertainty, syringe sampling error, and fit uncertainty.

### 2.4. Specific energy input and energy efficiency calculations

Electrical data were collected using a digital oscilloscope at 1 GS $s^{-1}$ over 10 plasma pulses. Current and voltage signals were phase-aligned using Python, and instantaneous power was computed pointwise ($P$ = IV). To manage data size, 1 in every 1000 points was sampled. Error was estimated by calculating the variance obtained from voltage and current arrays. Additional details regarding the energy data collection are provided in Section S1.4.

During each experiment, dissipated power was computed as follows:

$$P_{\text{diss}} = f \oint Q_{(\text{charge})} \mathrm{d}V \quad (1)$$

where $P$ represents the dissipated power in Joules per second, $f$ represents the frequency in Hertz, and $Q$ represents charge in Coulombs. $Q$–$V$ Lissajous plots for individual wavelengths were also made for each condition by plotting the voltage against the adjusted charge (Section S1.4). Error was calculated by adding the error in the frequency ($f_{\text{pulse}} = 35.5 \pm 0.5$ kHz) to the errors in the measured current and voltage. The frequency error was calculated by manually inspecting the number of wavelengths during a pulse for all conditions and taking the standard deviation.

Using the dissipated power values, SEI values were calculated by dividing the dissipated power by the flow rate using eqn (2), where $Q_{\text{flowrate}}$ represents the flow rate in liters per second.

$$\text{SEI}(\text{J} \cdot \text{L}^{-1}) = \frac{P_{\text{diss}}}{Q_{(\text{flowrate})}} \quad (2)$$

Energy efficiency values were then calculated using eqn (3), where $m$ represents the molar flow rates (moles per second), $\Delta H$ represents the enthalpy of molecules (eV $\text{mol}^{-1}$), and $P_{\text{supplied}}$ is the external power input (eV $s^{-1}$). The detailed procedure for calculating the molar flow rates, enthalpies, and external power is provided in Section S1.5.

$$\eta(\%) = \frac{m_{\text{co}} \Delta H_{\text{CO}_2} + m_{\text{H}_2} \Delta H_{\text{H}_2\text{O}}}{P_{\text{supplied}}} \quad (3)$$

### 2.5. Targeted reaction pathways

The conversion of $CO_2$ and $H_2O$ in non-thermal plasmas is thought to be initiated by electron-impact excitation and dissociation processes,[14] wherein energetic electrons selectively activate molecular vibrations or directly cleave chemical bonds. These interactions generate radicals and excited species[15] (*e.g.*, OH, O, H, $CO_2(v)$) that can recombine under non-equilibrium conditions to form stable products such as CO and $H_2$. As a result, the electron energy distribution function (EEDF) plays a central role in determining dominant reaction pathways and product selectivity.

In $CO_2$ conversion, low average electron energies preferentially promote vibrational excitation, enabling vibrational ladder climbing and eventual dissociation into CO and atomic O. At higher electron energies, direct electron-impact dissociation becomes accessible but can also enhance back-reactions that limit net CO formation. In contrast, $H_2O$ conversion proceeds primarily through direct electron-impact dissociation, producing hydrogen radicals that readily recombine to form $H_2$. Meanwhile, OH radicals produced from water dissociation can participate in secondary pathways or recombine to form water. The reaction pathways for $H_2O$ and $CO_2$ conversion are detailed in the SI (Section S1.6). When $CO_2$ and $H_2O$ are processed simultaneously, their chemistries become coupled through a shared radical pool. However, the extent to which SEI and flow rate jointly control CO and $H_2$ selectivity and energy efficiency in these systems remains underexplored, motivating the present study.

## 3. Results and discussion

### 3.1. Maximum energy conversion efficiencies yield the lowest syngas ratio

The effect of SEI on syngas conversion was initially investigated in a high $CO_2$ flow regime of 1.0 L $\text{min}^{-1}$. In this flow regime, energy efficiencies increased to a maximum of ~23% at an SEI of 2440 J $L^{-1}$ before gradually decreasing at higher SEI values (Fig. 1a). Consistent with expected energy utilization behavior, energy efficiencies exhibited a non-monotonic trend with SEI, peaking at intermediate values, and declining at both low and high SEI (Fig. 1a). Notably, the highest energy efficiency in this flow regime also generated the lowest syngas ratio due to high CO production (Fig. 1b). Overall, the relationship between syngas ratio and energy input did not demonstrate a declining linear trend as described in related literature.[4]

At the SEI that achieved the peak energy efficiency (2440 J $L^{-1}$), the CO concentration increased sharply (~+40% increase), whereas the $H_2$ concentration increased only marginally relative to the preceding condition (Fig. 1c and d). This divergence likely reflects a transition in the EEDF that increased the population of electrons energetic enough to dissociate $CO_2$, thereby enhancing CO formation and atomic oxygen production in the plasma. Although the population of electrons capable of dissociating $H_2O$ into $H_2$ would have also increased at this electron temperature, the observed increase in $H_2$ concentration was smaller than that for CO (Fig. 1c). This was likely because the excess atomic oxygen produced from $CO_2$ dissociation favored $H_2$ recombination pathways that reform $H_2O$, thereby suppressing net $H_2$ production. In contrast, CO was likely more stable due to its higher bond dissociation energy, allowing a larger fraction of CO molecules to persist as the gas exits the plasma zone. Consequently, the effluent gas exhibited an elevated CO concentration with only a modest increase in $H_2$, producing a local minimum in the syngas ratio. These phenomena are further discussed using simulation data in Section 3.6.

As SEI increases further beyond the point of the lowest syngas ratio, CO formation approaches a plateau (Fig. 1b and d). Beyond this point, additional increases in SEI no longer preferentially enhance CO formation, and $H_2$-producing pathways regain relative importance, leading to a subsequent increase in the syngas ratio (Fig. 1b–d). These observations may reflect the onset of CO dissociation at high SEI, reducing net CO production.

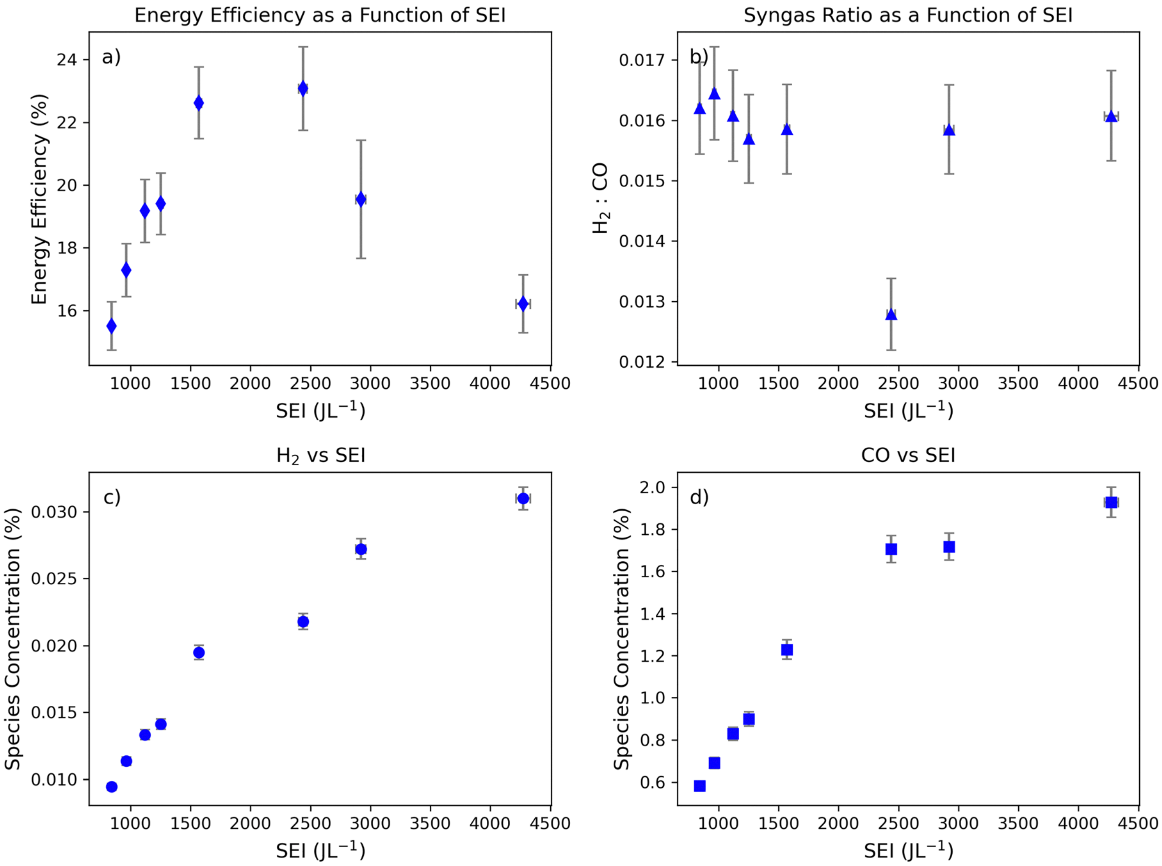

Fig. 1 Plasma-driven $H_2$/CO production in the high flow regime as a function of specific energy input. Energy efficiency as a function of SEI (A) and syngas ratios as a function of SEI (B) with errors in both dimensions. Observed $H_2$ (C) and CO concentrations (D) of the plasma effluent with errors in both dimensions. Influent gas flow rate of $Q$ = 1.00 L min$^{-1}$.

Interestingly, this saturation effect indicates that plasma ionization becomes less efficient beyond a critical SEI, with excess energy contributing to further bond dissociation. This interpretation is supported by the decline in energy efficiency observed beyond moderate SEI in this flow regime (Fig. 1a). However, the SEI range necessary to confirm the full extent of this plateau would require more complex testing equipment outside the scope of this study.

### 3.2. CO formation plateaus after the lowest syngas ratios are achieved

To further examine the effect of SEI on syngas formation, lower gas flow rates of 0.2 L min$^{-1}$ were applied to the DBD module (Fig. 2). The general trends in this moderate flow regime mirror those in the high-flow regime. Namely, the lowest syngas ratio ($H_2$/CO) occurs near the peak energy efficiency of the system (Fig. 1a and b). In addition, CO and $H_2$ production plateau at high SEI levels (Fig. 1c and d). As expected, the lowest syngas ratio (0.122 ± 0.005) occurs around 13 000 J L$^{-1}$, before the maximum SEI value in this regime.

The trends in SEI *versus* energy efficiency and $H_2$/CO ratio share some commonalities but differ in important ways (Fig. 2a and b). In general, both energy efficiency and the $H_2$/CO ratio decrease with increasing SEI. At high SEI, a larger fraction of the supplied energy was likely dissipated as heat or consumed in $CO_2$ or $H_2O$ recombination reactions, resulting in reduced energy efficiency (Fig. 2a). These observations are reflected in the relationship between SEI and syngas composition. At moderate SEI, elevated average electron temperatures promoted $CO_2$ dissociation to CO, resulting in a lower $H_2$/CO ratio (Fig. 2b). At the highest SEI (~27 500 J L$^{-1}$), however, enhanced $H_2O$ conversion to $H_2$ yields moderate $H_2$/CO ratios and reduced energy efficiencies despite CO formation having reached a plateau (Fig. 2b–d). These trends are consistent with those observed at higher flow rates and may reflect CO decomposition or a maximum in atomic oxygen generated during $CO_2$ dissociation, which favors $H_2$ reformation to $H_2O$.

Interestingly, the lowest SEI (~5000 J L$^{-1}$) also resulted in relatively low energy efficiency (~14%), likely because electron temperatures were insufficient to effectively dissociate either $H_2O$ or $CO_2$ during molecule-electron collisions. This interpretation is consistent with the low concentrations of both $H_2$ and CO measured under these conditions (Fig. 2c and d). However, as a higher fraction of electrons was likely capable of dissociating water, a high $H_2$/CO ratio was observed.

Beyond the lowest SEI, CO formation increases more rapidly than $H_2$ formation over the SEI range of ~5000–15 000 J L$^{-1}$. Although $H_2O$ is more readily dissociated than $CO_2$, its much

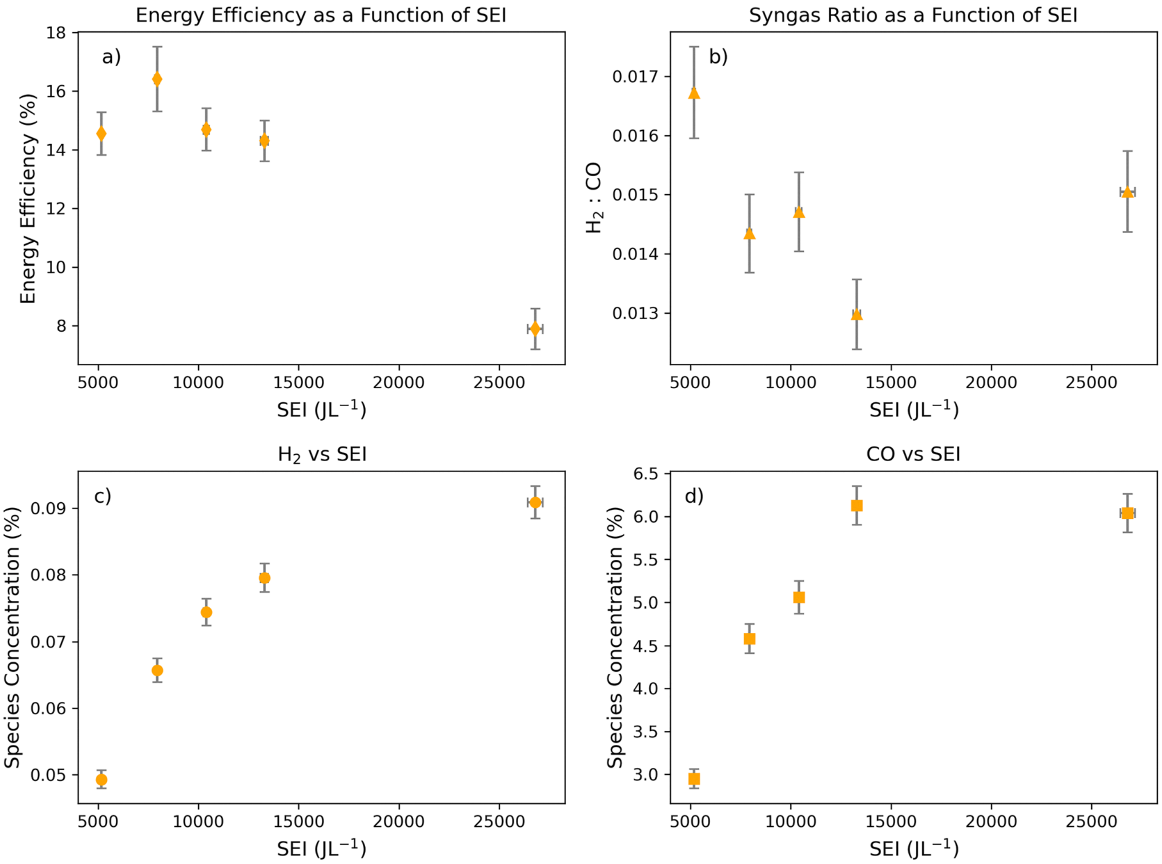

Fig. 2 Plasma-driven $H_2$/CO production in the medium flow regime as a function of specific energy input. Energy efficiency as a function of SEI (A) and syngas ratios as a function of SEI (B) with errors in both dimensions. Observed $H_2$ (C) and CO concentrations (D) of the plasma effluent with errors in both dimensions. Influent gas flow rate of $Q$ = 0.20 L min$^{-1}$.

lower concentration limits the relative increase in $H_2$ production. As a result, CO formation dominates, leading to a decrease in the $H_2$/CO ratio with increasing SEI. At an SEI of ~7900 J L$^{-1}$, energy efficiency reaches a maximum, coinciding with enhanced CO formation and a concurrent decline in the syngas ratio.

Proceeding to higher SEIs, CO and $H_2$ outputs increase only marginally despite substantial additional energy input (Fig. 2c and d), while overall energy efficiency declines, indicating that a growing fraction of input energy is diverted away from productive $H_2$/CO synthesis pathways. One plausible mechanism for this, beyond product dissociation, is that increased vibrational excitation (*e.g.*, OH stretch modes in $H_2O$) absorbs input energy without facilitating bond scission or productive recombination. However, advanced *in situ* or operando characterization techniques would be needed to verify such effects.

Accompanying tests at high and moderate gas flow rates, the effect of SEI on syngas formation was examined at ultra-low gas flow rates of 0.04 L min$^{-1}$ (Fig. 3). In general, this gas flow regime generated some of the clearest relationships between SEI, energy efficiencies, and product formation. This behavior may arise because the low flow rate enables the highest SEI to be reached, resulting in elevated electron temperatures and extended residence times that increase the likelihood of electron–molecule collisions.

As in previous flow regimes, the minimum syngas ratio was observed well below the highest SEI. In addition, CO and $H_2$ concentrations plateau at elevated SEI levels. Notably, an SEI of 23 300 ± 300 J L$^{-1}$ yields the lowest syngas ratio and occurs prior to the plateau in $H_2$ production, consistent with trends observed across other flow regimes. At this SEI, CO formation likely increases due to a rapid rise in the population of electrons capable of dissociating $CO_2$ (Fig. 3d). This enhanced $CO_2$ dissociation would result in a comparatively smaller increase in $H_2$ production due to the lower $H_2O$ concentration in the feedstock, consistent with the observed syngas ratios (Fig. 3b and c).

### 3.3. Flow rate and specific energy input impact energy efficiency

Comparing the results from different gas flow regimes shows that energy efficiency generally decreased as flow rates decreased (Fig. 4). However, higher flow rates generally yielded superior energy efficiencies at equivalent SEI values. These results highlight that SEI alone cannot reliably predict energy efficiency.

Interestingly, higher energy efficiencies were consistently observed at higher flow rates. For example, the maximum energy efficiency at 1.0 L min$^{-1}$ (~23%) was approximately 30% higher than that achieved at 0.2 L min$^{-1}$ (~16%), while the maximum efficiency at 0.2 L min$^{-1}$ was ~66% higher than

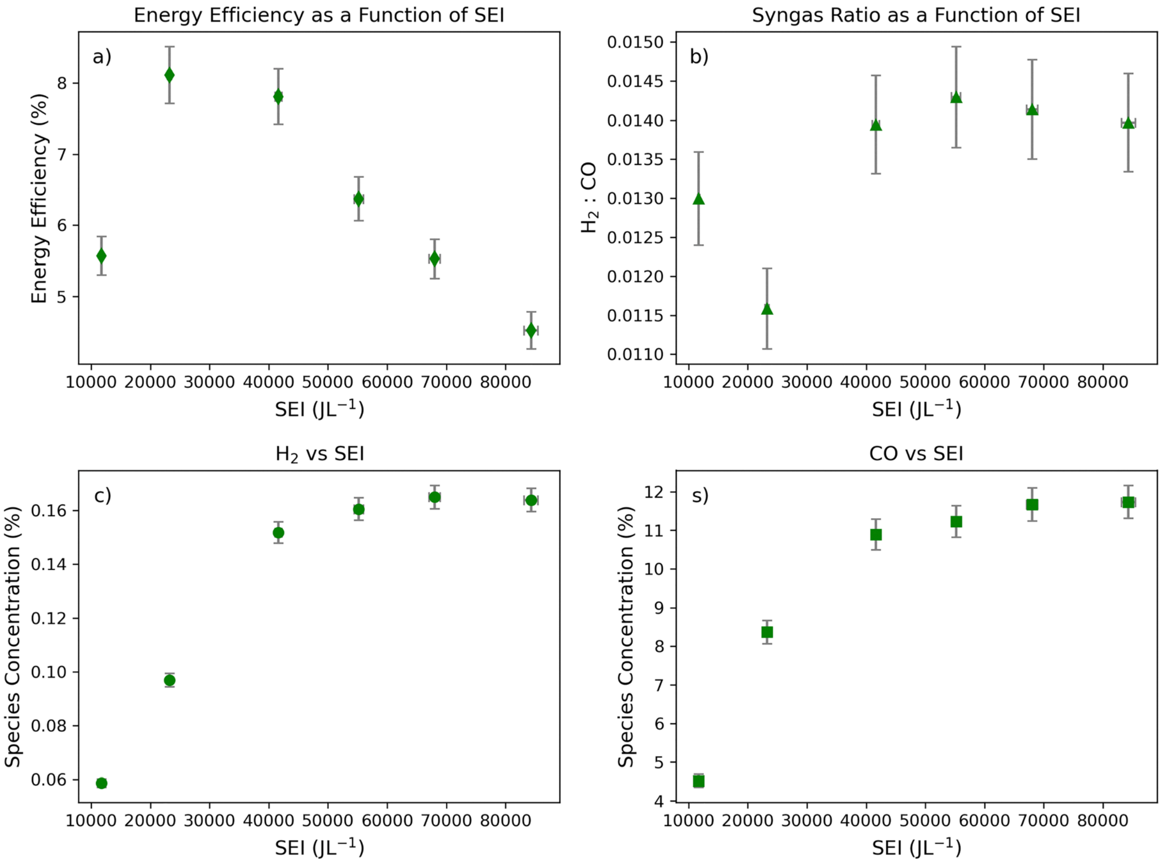

**Fig. 3** Plasma-driven $H_2$/CO production in the low flow regime as a function of specific energy input. Energy efficiency as a function of SEI (A) and syngas ratios as a function of SEI (B) with errors in both dimensions. Observed $H_2$ (C) and CO concentrations (D) of the plasma effluent with errors in both dimensions. Influent gas flow rate of $Q$ = 0.04 L min$^{-1}$.

that observed at 0.04 L min$^{-1}$ (Fig. 4). We attribute this trend to residence-time effects. At lower flow rates, residence times increase substantially (up to ∼48 s at 0.04 L min$^{-1}$), allowing gas-phase species to undergo many more plasma–molecule and electron–molecule collisions. Although this extended exposure enhances overall $CO_2$ conversion and product formation, it also increases the likelihood of non-productive secondary processes. In particular, species that have already formed (*e.g.*, $H_2$, CO) may undergo repeated dissociation, leading to wasted energy and reduced energy efficiency. As a result, low flow rates exhibit higher SEI and conversion but lower energy efficiency, whereas higher flow rates benefit from shorter residence times, fewer unnecessary collisions, and consequently higher energy efficiency. These phenomena likely led to the observed trend where energy efficiency generally decreases with increasing SEI across all flow regimes (Fig. 4). While additional flow rates (*e.g.*, 0.5 or 1.0 L min$^{-1}$) could have provided supplementary insights, other intermediate flow rates would have likely produced values closely clustered to the moderate flow rate tested. Furthermore, higher flow rates (>1.0 L min$^{-1}$) were constrained by the humidity control limitations and gas sampling requirements in our protocol. Because identical SEI values achieved *via* reduced flow or increased voltage can yield different plasma behaviors, SEI must be interpreted in the context of flow rate, residence time, gas composition, and pulse conditions. Future work could work to further decouple these effects by comparing identical SEI values reached through different operational pathways.

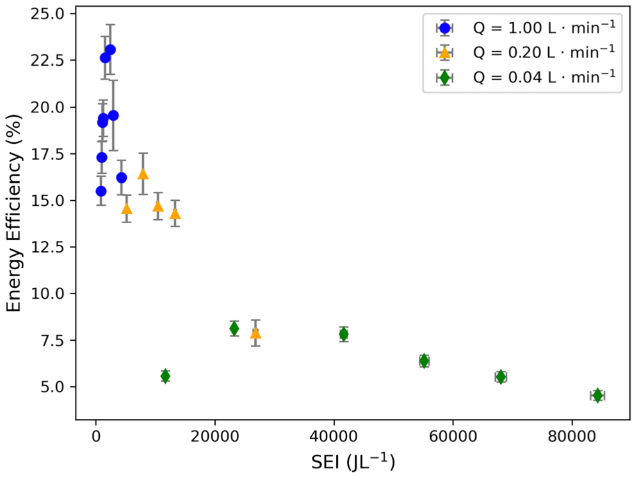

**Fig. 4** Comparison of energy efficiencies achieved for $H_2$/CO under different flow regimes. Energy Efficiency for $H_2$/CO production as a function of SEI and flow rate (markers).

### 3.4. Feedstock conversion and syngas ratio are influenced by flow rate and specific energy input

Building on the observation that SEI and flow rate impact energy efficiency, the role of these parameters on feedstock (*i.e.*, $H_2O$, $CO_2$) conversion and syngas ratio was analyzed (Fig. 5 and 6). Notably, feedstock conversion exhibits a clear and consistent dependence on SEI across all flow rates. $H_2O$ conversion increases with SEI before reaching a plateau (Fig. 5a), consistent with a logistic increase in the population of electrons with enough energy to dissociate $H_2O$. $CO_2$ conversion shows a similarly monotonic increase with SEI across flow regimes, followed by saturation at high SEI (Fig. 5b). This behavior likely reflects the increasing fraction of electrons capable of dissociating $CO_2$ as energy density rises, coupled with residence-time effects. Namely, high flow rates possibly yielded lower conversion due to shorter residence times and fewer productive molecule-electron collisions, whereas low flow rates seemed to promote higher conversion by extending plasma exposure (Fig. 5). A single deviation is observed under the lowest flow rate (0.04 L $\text{min}^{-1}$) and an SEI of 23 300 ± 300 J $L^{-1}$. This point coincides with the lowest syngas ratio and the highest carbon deposition (Fig. S5), suggesting the involvement of additional pathways such as CO dissociation or surface-mediated processes. Resolving this behavior will require advanced spectroscopic investigation outside the scope of the current study. Overall, this analysis of feedstock conversion reinforces that increasing SEI (*via* higher power and/or longer residence time) raises electron temperature and conversion until a plateau is reached, beyond which additional energy no longer yields proportional gains. This interpretation is supported by the simulations discussed in Section 3.6 and underpins the observed relationships between SEI and syngas ratio (Fig. 6).

The results of this study demonstrate the ability to tune syngas ratios from around 0.011 to 0.016 by adjusting SEI and flow rate (Fig. 6a). In general, there is no clear difference between the syngas ratios achievable at different flow rates. While the lowest flow rate demonstrates the lowest syngas ratio of 0.011, this condition seemed to be an outlier. Altogether, this study draws different conclusions about the relationship between increased power applied and syngas ratios than the study conducted by Snoeck *et al.* 2017, which noted that the syngas ratio ($H_2 : CO$) decreases with energy input.[4] This could be due to differences in the DBD reactor architecture between our study and past work. Notably, this study also observed that the minimum syngas ratio occurs well below the maximum applied power and plateau behavior of CO (Fig. 1–3). Similarly, all but these outlying minimum syngas experiments have overlapping error bars, meaning that there is not a clear linear relationship between the syngas ratio and energy input as might be expected based on the activation energies of $CO_2$ and $H_2O$.

Notably, while many operating conditions can yield similar syngas ratios ($H_2/CO$), the absolute amounts of $H_2$ and CO produced in the plasma can differ substantially. Consequently, experiments with comparable syngas ratios may nonetheless exhibit distinct overall gas compositions. This behavior reflects the fact that the syngas ratio primarily captures reaction pathway selectivity rather than absolute product yields. Changes in flow rate mainly affect residence time and, therefore, the extent of reaction, allowing $H_2$ and CO production to scale together under similar discharge conditions while maintaining a nearly constant ratio. As a result, comparable $H_2/CO$ ratios can be obtained at different flow rates despite large differences in absolute $H_2$ and CO concentrations. This effect can be illustrated by plotting the syngas ratio as a function of $H_2$ and CO concentration (SI Section and Fig. S6, S7), which demonstrates that similar syngas ratios can arise from markedly different product CO and $H_2$ yields under distinct operating conditions.

Plotting syngas ratio with respect to the dissipated power does not support a negative trend as might be expected based on SEI trends (Fig. 5b). Instead, similar dissipated power applied under different flow rates can yield either comparable or distinct syngas ratios. One explanation is that similar electron temperatures may

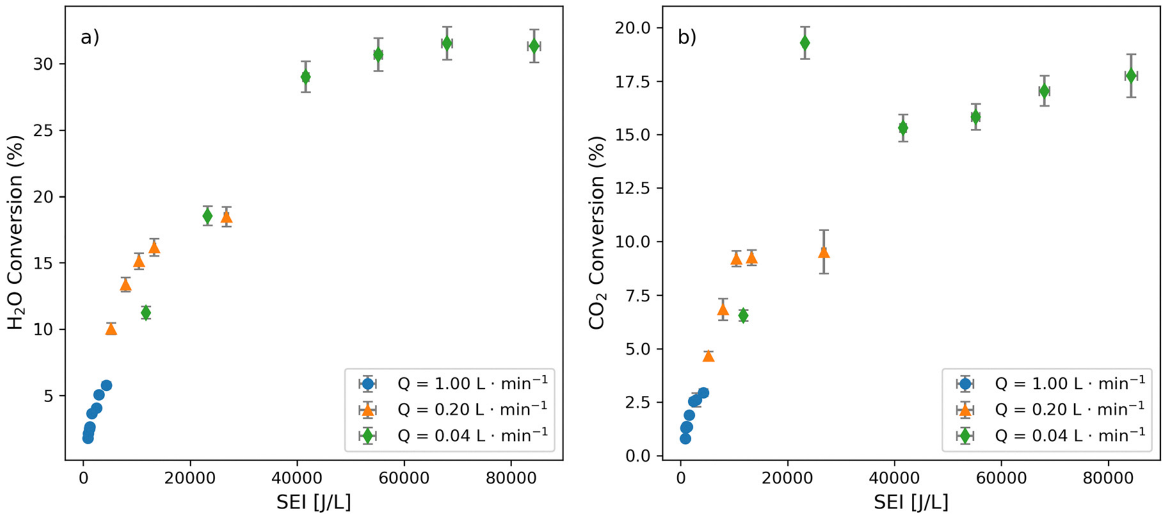

Fig. 5 Conversion of (a) $H_2O$ and (b) $CO_2$ as a function of specific energy input (SEI) at different volumetric flow rates in the DBD reactor. Data are shown for humidified $CO_2$ flow rates of 1.00, 0.20, and 0.04 L $\text{min}^{-1}$, corresponding to residence times of 1.9, 9.6, and 4 s, respectively.

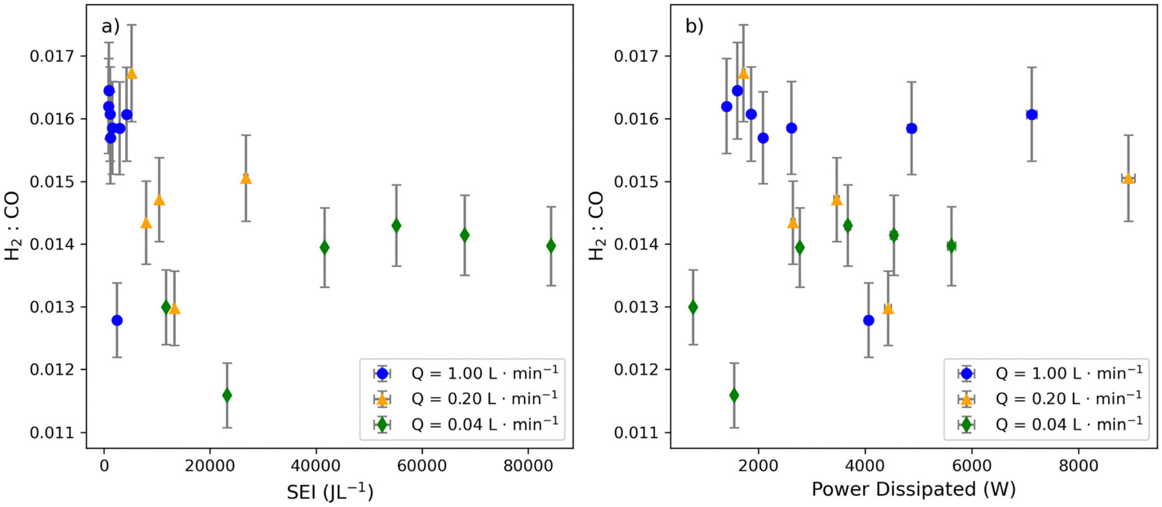

Fig. 6 Comparison of syngas ratios across flow regimes. Syngas ratios as a function of SEI (A) syngas ratio as a function of dissipated power (B), with influent gas flow rates as markers.

be achieved under different operating conditions, leading to comparable reaction selectivity. For example, when electron temperatures are sufficient to maximize $H_2O$ dissociation, both high- and low-flow regimes can generate similar hydrogen radical concentrations and thus comparable recombination behavior upon exiting the plasma. However, differences in residence time can truncate reaction pathways at higher flow rates, resulting in divergent product distributions even at similar applied power. Consistent with this interpretation, at comparable power the 1.00 L $min^{-1}$ condition exhibits significantly higher syngas ratios than the 0.04 L $min^{-1}$ condition, reflecting its ∼25-fold shorter residence time (Fig. 6b). These results indicate that syngas formation is governed not only by electron temperature but also by residence time. Together, they establish a more nuanced relationship between syngas ratio, residence time, and energy input, providing a refined framework for interpreting plasma-driven syngas formation and guiding future studies.

### 3.5. Simplistic computational modeling and reasoning

To better understand the underlying reactions of the DBD plasma system, modeling of simplistic electron energy distribution functions was performed and compared to the relevant bond dissociation energies of molecules in the humidified $CO_2$ feed gas (Fig. 7 and Table 1). A Druyvesteyn distribution was used to depict the plasma, which has more electrons with energies near the average kinetic energy and a less voluminous high-energy tail than a Maxwell–Boltzmann distribution.[3] As such, the Druyvesteyn distribution has been found to more accurately describe plasmas that are not in local thermodynamic equilibrium.[3,15]

As expected, the EEDF model predicts that greater electron temperatures yield higher energy electrons (Fig. 6). When electrons with energy greater than a bond energy collide with a heavy molecule like $CO_2$, there is a chance that the collision causes the molecule to dissociate into quasi-stable products (*e.g.*, CO, O). When the electron temperature is sufficiently high, almost all electrons are well above the dissociation energy of a molecule like $H_2O$, leading to a high probability of $H_2O$ dissociation alongside $CO_2$ conversion. Conversely, at low electron temperatures where very few electrons have enough energy to dissociate a molecule like $CO_2$, as a consequence, fewer $CO_2$ dissociation reactions are expected. Accordingly, EEDF models combined with an understanding of molecular structure can help interpret many of the results from this study.

A common trend across all gas flow rate regimes was an increase in $H_2$ and CO formation up until a plateau at high SEIs (Fig. 1–3). Based on bond dissociation energies of the feedstock molecules, it would be expected that the first reaction to occur at low electron temperatures would be $H_2O$ dissociation to $H_2$ (4.77 eV, Table 1). As electron temperatures increase, it would then be expected that $H_2$ decomposition (5.18 eV) could occur, followed by $CO_2$ decomposition into CO (6.35 eV), and finally CO decomposition (11.23 eV). Accordingly, it is expected that increasing the average electron temperature by increasing SEI would enhance $H_2$ and CO formation up until the decomposition reactions of these molecules take place, leading to a semi-equilibrium and plateau of their concentrations in the effluent plasma. This logic aligns the trends observed across all the flow regimes tested (Fig. 1–3) and is consistent with the EEDF simulation results (Fig. 7 and 8). For example, at a low electron temperature ($T_e$ = 3.00 eV), approximately 16% of electrons can drive $H_2$ formation, ∼12% can dissociate $H_2$, ∼5% can convert $CO_2$ to CO, and virtually none can dissociate CO. In contrast, at a higher electron temperature ($T_e$ = 7.50 eV), these fractions increase to ∼67%, ∼64%, ∼53%, and ∼20%, respectively (Fig. 7). Thus, increasing electron temperature beyond a critical threshold is expected to inhibit $H_2$ and CO formation, as observed in this study with increasing SEI (Fig. 1–3).

Overall, these mechanisms likely contributed to the relationship between SEI and energy efficiency across all flow regimes analyzed in this study. For each flow rate, energy efficiency initially increases with SEI, reaches a maximum, and then decreases at higher SEI values (Fig. 4). However, $H_2O$ and $CO_2$ conversion were found to rise with increasing SEI before

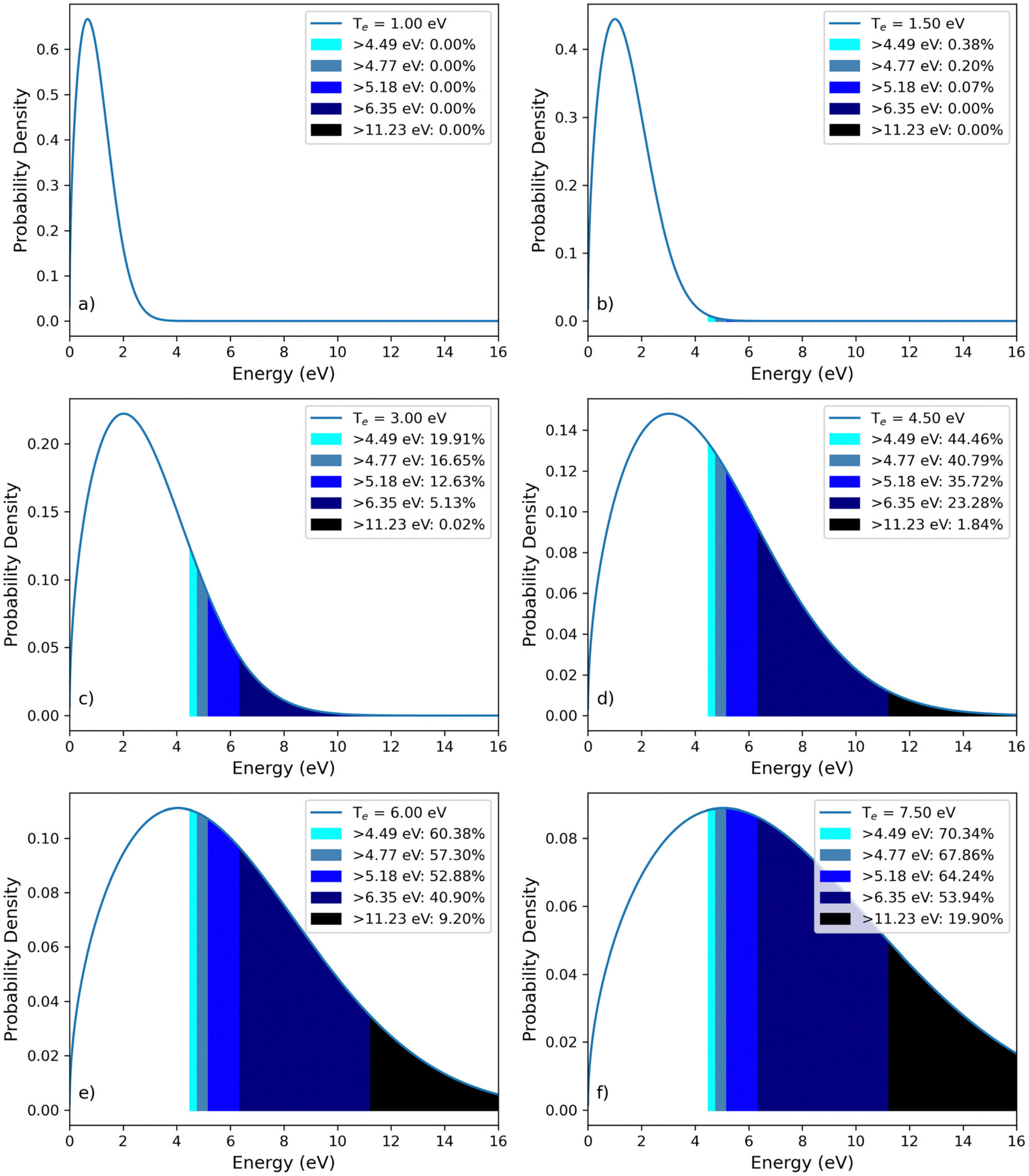

Fig. 7 Druyvesteyn electron energy distributions during syngas formation. Predicted electron density or fraction (*y*-axis) *versus* electron energy (eV). Electron energy and percentage distribution for each bond activation zone are shown in each legend. The lightest blue shade in the legend represents the percentage of electrons with kinetic energy above the bond energy of $H_2$. The next-lightest shade of blue represents electrons with kinetic energy greater than O–H bonds in OH and $H_2O$. The dark blue area represents electrons with kinetic energy greater than the $C{=}O$ bond strength of $CO_2$. The purple shade represents electrons with kinetic energy greater than the $C{\equiv}O$ bond strength of CO. The activation energies[16] of $H_2$ (4.49 eV), $H_2O$ (4.77 eV), OH (4.77 eV), $O_2$ (5.18 eV), $CO_2$ (6.35 eV), and CO (11.23 eV) define each shaded region. The effective electron temperature increases in each plot from 1.00 eV in Panel a to 7.5 eV in Panel f.

reaching a plateau at elevated SEI (Fig. 5). These observations suggest that after a significant population of electrons becomes capable of dissociating $H_2$ and CO, increasing SEI promotes further $H_2O$ and $CO_2$ conversion while decreasing energy efficiency due to increased electron-impact destruction of the products. This rationale tracks with trends observed in the EEDF simulation data. As an example, at an electron temperature of 4.5 eV, ~35% of electrons have sufficient energy to dissociate $H_2$, and ~2% can dissociate CO. However, increasing the electron temperature to 6.0 eV nearly doubles the fraction capable of dissociating $H_2$ and increases the fraction capable of dissociating CO by a factor of five (Fig. 8a). Accordingly, at high SEI, we would expect reduced net $H_2$ and CO yields even if $H_2O$ and $CO_2$ dissociation increase.

**Table 1** Relevant bond energies of reactants and products. Electron energies shown in the second column from left are the dissociation energies of the bonds shown in the third column. The parent molecule, shown in the second column from the right, dissociates into the products on the rightmost column when enough energy is applied to the bond. Bond energy values adapted from ref. 17

| Bond | Energy (eV) | Parent molecule | Products |
|---|---|---|---|
| C=O | 6.35 | $CO_2$ | CO, O |
| O–H | 4.77 | $H_2O_4$ | OH, H |
| O–H | 4.77 | OH | O, H |
| H–H | 4.49 | $H_2$ | H, H |
| C≡O | 11.23 | CO | C, O |
| O=O | 5.18 | $O_2$ | O, O |

Product decomposition informed by EEDF also helps explain the observed dependence of the syngas ratio on SEI. Across all flow regimes tested, the minimum syngas ratio was found to occur at intermediate SEI, well below the maximum SEI (Fig. 1–4). Notably, the minimum syngas ratio is observed before $H_2$ production plateaus, and well before the maximum syngas ratio in each regime. This minimum often coincides with peak energy efficiency, reflecting preferential enhancement of CO formation relative to $H_2$. These phenomena are predicted by EEDFs as a result of an increase in $CO_2$ dissociation reactions that occurs at a slightly higher electron temperature than the dissociation of $H_2O$. This results in O radicals, which can consume H atoms. When an H-containing molecule combines with an O-containing molecule, the stoichiometric balance is shifted towards less $CO_2$, leading to more CO and less $H_2$. Based on previous studies, it is expected that minimum syngas ratios would occur at SEI values before a plateau in CO formation. This notion is reinforced by comparing the number of electrons capable of dissociating one bond relative to another at different electron temperatures (Table 1 and Fig. 7).

Accordingly, combining experimental and modeling data can predict ideal operating conditions for target syngas ratios. For example, EEDF simulations indicate there is an electron temperature window where the ratio of electrons with energy levels greater than the bond energy of $H_2O$ far exceeds those with energy levels greater than the bond energy of $CO_2$ (Fig. 8b). Therefore, targeting this electron temperature is predicted to produce high syngas ratios under low SEI conditions. These conditions could be ideal for some real-world operations and are supported by the results of this study across operating flow rates (Fig. 1–4). Conversely, these models can also predict electron temperatures where both $H_2O$ and $CO_2$ dissociation are high, leading to a large number of free O radicals that capture H to form OH and $H_2O$. This mechanism could limit the reformation of $H_2$ and lead to a minimum syngas ratio, which could be ideal in some industrial scenarios. As such, beyond helping to interpret the results of this study, these computational models can help guide future research and plasma applications.

## 4. Conclusions

This study investigated syngas production under different flow regimes using a coaxial DBD reactor and humified $CO_2$ gas. This work aimed to clarify the relationship between syngas ratios and SEI under different flow rates to provide a foothold for future studies to expand upon. Notably, experiments showed that contrary to other works,[4] there was no clear decrease in produced syngas ratios with increasing energy input. Instead, minimum syngas ratios in each flow regime were produced before the maximum applied SEI.

To better understand the mechanisms behind these results, this study employed a simplistic computational model for predicting and understanding syngas production achieved under different SEIs and gas flows. The EEDF model supports that conditions can be found that heavily favor the dissociation of some molecules and not others, leading to fluctuations in produced syngas ratios.

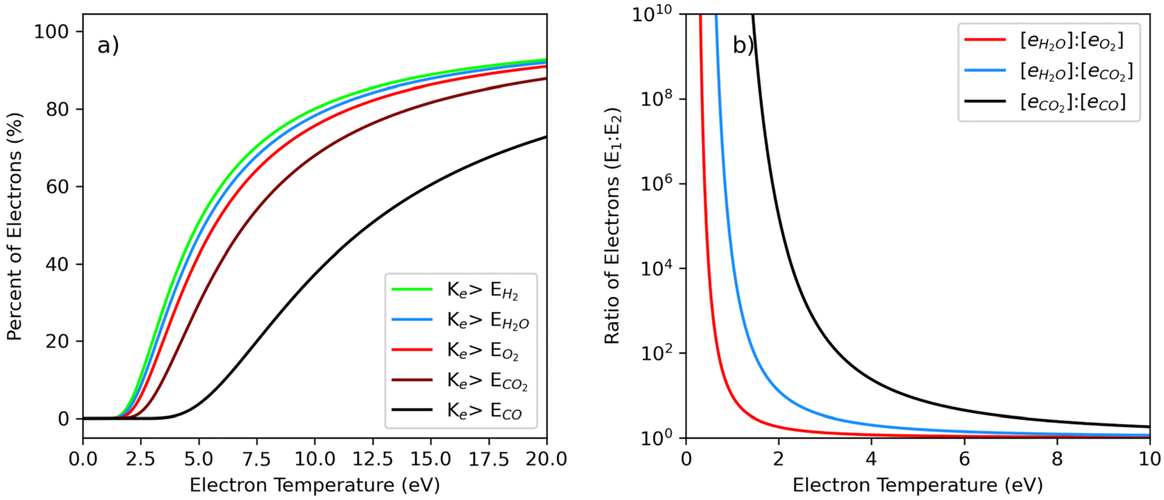

**Fig. 8** Electron energy distributions as a function of electron temperature. The estimated percentage of electrons with a kinetic energy ($K_e$) above a bond dissociation energy for a given molecule ($E_x$), referenced in the legend. (a) For example, at $T_e$ = 10 eV, 70% of electrons have energies higher than the bond energy of $CO_2$. The estimated ratio of electrons ($E_1:E_2$) *versus* electron temperature (eV) (b). Colors depict the ratio of electrons above one energy level compared to the number of electrons above a higher energy level. For example, the ratio of electrons with energy levels greater than the bond energy of $H_2O$ relative to electrons with energy levels greater than the bond energy of $CO_2$ is shown in the blue line.

Furthermore, combining experiment and computational results reveals a more complicated relationship between syngas ratio and SEI than previously described.[4] While other studies have explored the relationship between SEI and product gases in a DBD reactor,[18] this study is among the first to use SEI as the independent variable for syngas production and energy efficiency in a silent DBD reactor for the reduction of $CO_2$ and $H_2O$.

Overall, this study provides a roadmap of syngas ratios and associated energy efficiencies under different operational conditions. We expect that this data can be used in future studies to help tune syngas ratios to match market-specific needs[4] and downstream applications such as Fischer–Tropsch synthesis of sustainable fuels. Although it was not the core focus of this study, this work also achieved an impressive maximum energy efficiency of 23 ± 1%. Building on this study, future studies could work toward highly efficient reactors capable of creating desired syngas blends. As such, this work sets the stage for NTP to be used in multiple sectors of the energy economy to achieve net-zero emissions through efficient $CO_2$ valorization.

## Author contributions

Conceptualization: JJ. Formal analysis: MK. Funding acquisition: JJ. Investigation: MK and JJ. Methodology: MK and JJ. Project administration: JJ. Resources: JJ. Supervision: JJ. Visualization: MK. Writing – original draft: MK and JJ. Writing – review & editing: MK and JJ.

## Conflicts of interest

There are no conflicts to declare.

## Data availability

The datasets supporting this article have been included as part of the supplementary information (SI). The SI includes additional details on the reactor setup as well as supplemental calculations and analyses. Further information that is not provided can be obtained from the authors upon request. Supplementary information is available. See DOI: https://doi.org/10.1039/d5ya00293a.

## Acknowledgements

JJ and MK acknowledge financial support provided by the University of Michigan's College of Engineering and Michigan Institute for Plasma Science and Engineering.

## References

1 Intergovernmental Panel on Climate Change, *Climate Change 2022: Mitigation of Climate Change*, https://www.ipcc.ch/report/ar6/wg3/chapter/technical-summary/, (2022).
2 S. Barbhuiya, F. Kanavaris, B. B. Das and M. Idrees, Decarbonising cement and concrete production: Strategies, challenges and pathways for sustainable development, *J. Build. Eng.*, 2024, **86**, 108861.
3 A. Grill, Fundamentals of Plasma, *Cold Plasma Materials Fabrication: From Fundamentals to Applications*, IEEE, 1994, pp. 1–23, DOI: 10.1109/9780470544273.ch1.
4 R. Snoeckx, A. Ozkan, F. Reniers and A. Bogaerts, The Quest for Value-Added Products from Carbon Dioxide and Water in a Dielectric Barrier Discharge: A Chemical Kinetics Study, *ChemSusChem*, 2017, **10**, 409–424.
5 P. L. Spath and D. C. Dayton, Preliminary Screening – Technical and Economic Assessment of Synthesis Gas to Fuels and Chemicals with Emphasis on the Potential for Biomass-Derived Syngas, (2003).
6 Z. Cui, *et al.*, Plasma-Catalytic Methanol Synthesis from CO2 Hydrogenation over a Supported Cu Cluster Catalyst: Insights into the Reaction Mechanism, *ACS Catal.*, 2022, **12**, 1326–1337.
7 S. Futamura and H. Kabashima, Synthesis Gas Production from $CO_2$ and $H_2O$ with Nonthermal Plasma, ed. Park, S.-E., Chang, J.-S. & Lee, K.-W., in *Studies in Surface Science and Catalysis*, Elsevier, vol. 153, 2004, pp. 119–124.
8 Nonthermal Plasma-Assisted $CO_2$-$H_2O$ Conversion over NiO and $Co_3O_4$ Supported on $CeO_2$ - Bajpai - 2023 - Chemical Engineering & Technology - Wiley Online Library. https://onlinelibrary.wiley.com/doi/10.1002/ceat.202200481.
9 X. Yao, Y. Zhang, Z. Wei, M. Chen and W. Shangguan, Plasma-Catalytic Conversion of CO2 and H2O into H2, CO, and Traces of CH4 over NiO/Cordierite Catalysts, *Ind. Eng. Chem. Res.*, 2020, **59**, 19133–19144.
10 Anonymous. Plasma-Assisted Catalytic Reverse Water Gas Shift Reactor. *Tech Briefs* **41**, (2017).
11 S. Mahammadunnisa, E. L. Reddy, D. Ray, C. Subrahmanyam and J. C. Whitehead, CO2 reduction to syngas and carbon nanofibres by plasma-assisted *in situ* decomposition of water, *Int. J. Greenhouse Gas Control*, 2013, **16**, 361–363.
12 A. Indarto, D. R. Yang, J.-W. Choi, H. Lee and H. K. Song, Gliding arc plasma processing of CO2 conversion, *J. Hazard. Mater.*, 2007, **146**, 309–315.
13 G. Chen, *et al.*, Simultaneous dissociation of CO2 and H2O to syngas in a surface-wave microwave discharge, *Int. J. Hydrogen Energy*, 2015, **40**, 3789–3796.
14 R. Aerts, W. Somers and A. Bogaerts, Carbon dioxide splitting in a dielectric barrier discharge plasma: a combined experimental and computational study, *ChemSusChem*, 2015, **8**, 702–716.
15 X. Ma, *et al.*, Plasma Assisted Catalytic Conversion of CO2 and H2O Over Ni/Al2O3 in a DBD Reactor, *Plasma Chem. Plasma Process.*, 2019, **39**, 109–124.
16 R. J. Carman and R. P. Mildren, Electron energy distribution functions for modelling the plasma kinetics in dielectric barrier discharges, *J. Phys. Appl. Phys.*, 2000, **33**, L99.
17 P. Flower, K. Theopold, R. Langley and A. Christianson 9.4: Bond Strength and Energy. *Chemistry LibreTexts* https://chem.libretexts.org/Courses/Bellarmine_University/BU%3A_Chem_103_(Christianson)/Phase_3%3A_Atoms_and_Molecules_-_the_Underlying_Reality/9%3A_Chemical_Bonding/9.4%3A_Bond_Strength_and_Energy (2018).
18 S. Müller, *et al.*, Investigation of Partial Oxidation of Methane in a Cold Plasma Reactor with Detailed Product Analysis, *Plasma Chem. Plasma Process.*, 2023, **43**, 513–532.